

Mixing across the Pacific

J. A. MACKINNON¹, M. H. ALFORD², ROB PINKEL³, JODY KLYMAK⁴, AND ZHONGXIANG ZHAO⁵

¹*Scripps Institution of Oceanography, La Jolla, CA, USA.*

²*Applied Physics Laboratory and School of Oceanography, University of Washington, Seattle, WA, USA*

³*Scripps Institution of Oceanography, La Jolla, CA, USA.*

⁴*University of Victoria, Victoria, British Columbia, Canada*

⁵*Applied Physics Laboratory, University of Washington, Seattle, WA, USA*

ABSTRACT

Turbulent mixing rates are inferred from measurements spanning 25–37° N in the Pacific. The observations were made as part of the Internal Waves Across the Pacific experiment, designed to investigate the long-range fate of the low-mode internal tide propagating north from Hawaii. Previous and companion results argue that near a critical latitude of 29° N, the internal tide loses energy to high-mode near-inertial motions through parametric subharmonic instability. Elevated shear at that latitude lead to estimates of significantly elevated turbulent mixing, based on finescale shear parameterizations of mixing. Here we estimate mixing from several variations of the finescale method, as well as Thorpe analysis of overturns. Turbulent diffusivity rates estimated from either Thorpe scale analysis or finescale strain predict only a modest elevation at and south of the critical latitude. Reasons for the discrepancy are discussed.

1. Introduction

Away from surface and bottom boundary layers the magnitude and geography of diapycnal mixing in the ocean interior is largely set by the dynamics of breaking internal gravity waves. Over the last two decades it has become clear that wave breaking, and the resultant turbulent mixing, are strongly inhomogeneous in both space and time (Kunze *et al.* 2006) (hereafter K06). The patterns are driven by details of internal wave generation, propagation, interaction, and dissipation. In turn, the patchiness of diapycnal mixing has significant consequences for both regional and global flow patterns (Jochum and Potemra 2008; Harrison and Hallberg 2008; Jayne 2009). Current generation climate models include little if any of these patterns; improvement requires both a better map of where mixing is happening and a better dynamical understanding of why, so that mixing may be incorporated in models of both present and future climate (Wunsch and Ferrari 2004).

Much recent work has focused on striking patterns of elevated mixing near the generation sites of internal tides (Polzin *et al.* 1997) or wind-driven near-inertial waves (Alford and Gregg 2001). Internal tides are generated where the barotropic tide flows over rough topography, generating internal waves on a variety of scales. Waves with smaller vertical scales tend to break nearby, producing a global pattern of mixing hotspots that resembles a map of internal tide generation (St. Laurent *et al.* 2002; Polzin 2004). However, most generated internal

wave energy escapes to radiate up to thousands of km away; where and how these waves break is as yet unknown (St. Laurent and Garrett 2002). As a community we are challenged to map ‘farfield’ patterns of energy loss from the propagating component of the tide and associated patterns of mixing across ocean basins. Candidates for wave dissipation include scattering off deep-sea topography (Johnston *et al.* 2003) or reflection and wave breaking at the continental shelf break (Nash *et al.* 2004, 2007; Martini *et al.* 2011; Kelly *et al.* 2011). Alternately, a propagating internal tide can steadily lose energy through nonlinear interactions with other waves or mesoscale features (Gregg 1989; Polzin 2008). Differentiating between these candidates is an essential part of developing proper understanding and parameterizations of mixing. Part of the difficulty in differentiating the role of each mechanism is the relative sparseness of mixing observations (Gregg 1998), the most accurate of which are expensive and require specialized microstructure programs. Recent techniques that allow rough estimates of the turbulent mixing rate from finescale measurements of shear and strain have considerably broadened the available data, though great care must be taken in interpreting the results (K06).

The Internal Waves Across the Pacific (IWAP) experiment was designed to investigate the long-range fate of a propagating low-mode internal tide through a combination of moored arrays, spatial surveys and intensive time series (Fig. 1). One of the leading hypotheses was that the tide would lose significant energy to small-scale mixing through parametric subharmonic instability (PSI) near a critical latitude of 29° N (Hibiya and Nagasawa 2004;

Corresponding author address: J.A. MacKinnon, 9500 Gilman Dr., Mail Code 0213, La Jolla, CA. E-mail: jmackinnon@ucsd.edu

MacKinnon and Winters 2005; Young *et al.* 2008). Preliminary results in Alford *et al.* (2007) demonstrated that while there was clear evidence of PSI near 29N, it did not catastrophically drain energy from the internal tide. In fact, the tide propagates coherently for huge distances across the Pacific (Zhao *et al.* 2010). Further analysis of PSI from the observations is presented in a companion paper (MacKinnon *et al.* 2011), hereafter M11a.

Here we present detailed estimates of the turbulent mixing rate across 12 degrees of latitude. The measurements are described in Section 2. The following section goes through the basic theory underlying various methods to estimate mixing. We conclude with a comparison between methods and a discussion of the overall patterns and mixing level observed.

2. Instrument and experimental design

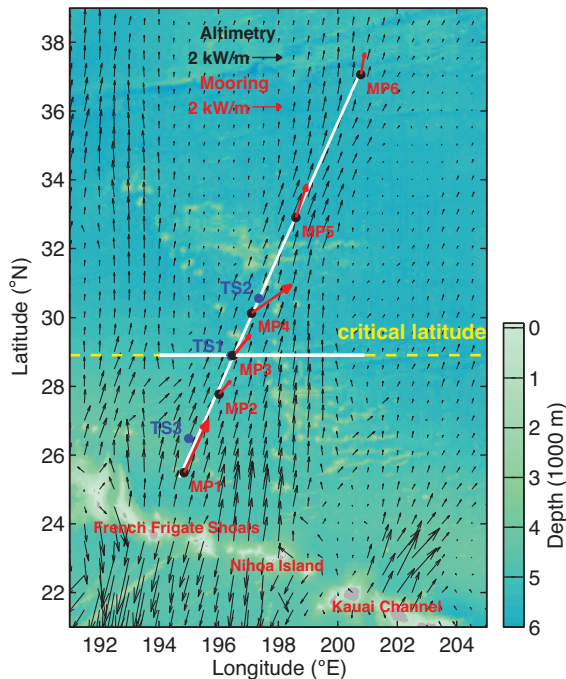


FIG. 1. Bathymetry (colors; axis at lower right), measurement locations (black, moorings; blue, shipboard time series; white, ship track), and internal-tide energy fluxes (black, altimetry estimates from Zhao and Alford (2009); red, mooring estimates from Zhao *et al.* (2010)). The critical latitude for the M_2 subharmonic, 28.8N, is indicated with a dotted line.

The following observations were made over a 60 day period encompassing two cruises aboard *R/V Revelle* during spring 2006:

a. Moored Profiler Array

Six moorings were deployed at locations shown in Figure 1 (labeled MP1-MP6) for 50 day timeseries. A McLane Moored Profiler on each mooring crawled from 85-1400 m every 1.5 hours (each way) measuring tem-

perature, salinity, and horizontal velocity (Doherty *et al.* 1999). MP4 stopped profiling after 23 days owing to a broken drive axle, and MP5 did not sample the upper 400 m after about 5 days owing to heavy ballasting. Each profiler was equipped with an Acoustic Current Meter and CTD from Falmouth Scientific. Corrections were made for mis-matched temperature and conductivity cells following Lueck and Picklo (1990). In order to remove residual sensor noise, temperature and conductivity data were smoothed to 3 m. Velocity data were smoothed to 0.1 cpm. The filtered density has an approximate noise level of $6 \times 10^{-4} \text{ kg m}^{-3}$. Figure 2 shows an example of the zig-zag pattern of MMP measurements in depth and time.

b. Spatial velocity surveys

Two northward and two southward 1400-km transits of the line were conducted from 25-37°N, as well as an eastward transit along 28.8N (Fig. 1, white). Velocity and shear were measured using *Revelle's* Hydrographic Sonar System (HDSS). A 50-kHz system measured velocity in 8-m vertical bins. When underway the along-ship velocity was contaminated by strong backscatter gradients due to patches of plankton, hence while steaming only velocity and shear in the cross-ship direction are used (Pickering *et al.* 2011). To remove a noise floor as seen in spectral analysis, data are filtered to 0.03 cpm.

c. High resolution time series

Intensive time series were conducted with a Fast CTD (FCTD) developed by R. Pinkel. Four-day time series were made in three locations (TS1-3 in Figure 1, numbered in order of occupation). The profiler measures temperature and conductivity down to 1000 meters ever 10 minutes. FCTD data are also corrected for sensor mismatch, and low-pass filtered to 0.5 m. The filtered density has an approximate noise level of $3 \times 10^{-4} \text{ kg m}^{-3}$. The shipboard HDSS sonar system was also operational during these time series, measuring both components of horizontal velocity down to 1000 meters (Fig. 2, lower panel).

3. Methods of estimating mixing

A common (if overly simplified) picture of turbulence in the stratified ocean is of a downscale cascade of energy - from low to high wavenumber internal waves through wave-wave interactions (McComas and Müller 1981b), to stratification-limited turbulent overturns, through a turbulent inertial subrange, to viscous dissipation at mm scales (Staquet and Sommeria 2002; Polzin 2004). The process is sketched schematically in Figure 3. The rate of energy dissipation at the smallest scales, ϵ , is typically used as a measure of the strength of the turbulence, and can in turn be related to the turbulent diffusivity by

$$K_p = \Gamma \frac{\epsilon}{N^2} \quad (1)$$

where Γ is a mixing efficiency, typically taken to be

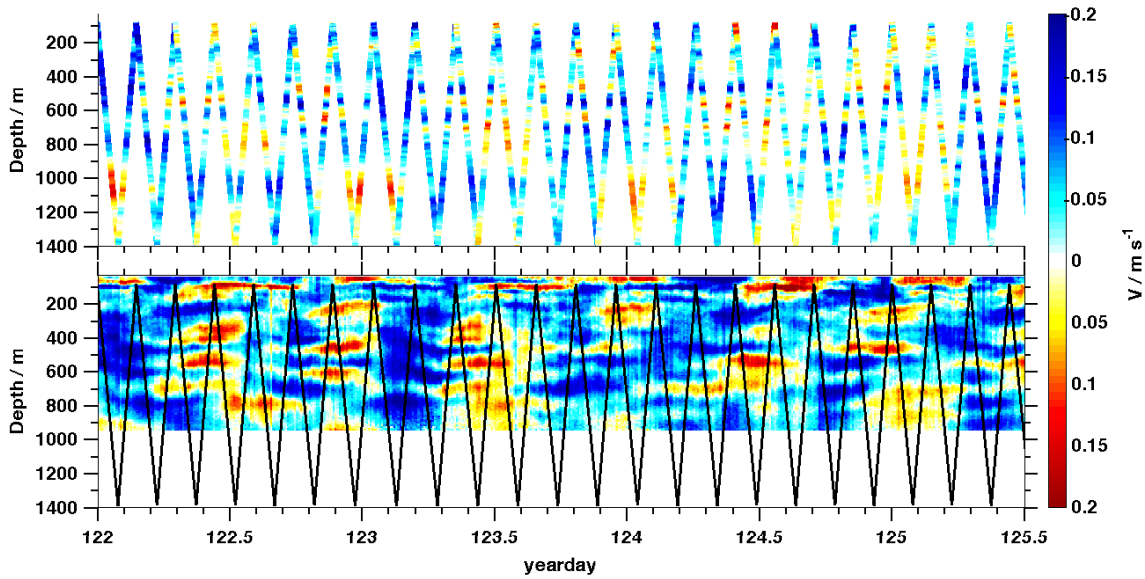


FIG. 2. A comparison of north-south velocity measured during the four-day time series at TS1 from the MMP (upper) and HDSS (lower). The zig-zag time-depth sampling of the MMP is indicated by the location of data in the top panel and also a black line in the lower panel.

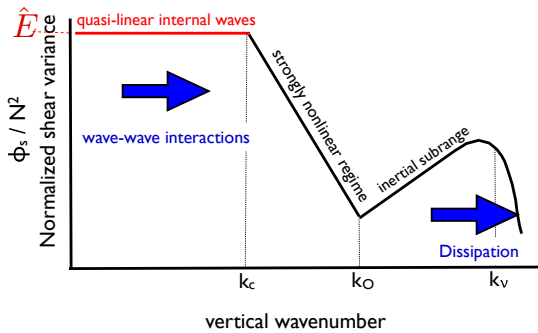


FIG. 3. Sketch of idealized vertical wavenumber spectra of stratification normalized shear showing steady-state spectral shapes for the internal wave regime (low wavenumbers / large vertical scales), the transition range, and the turbulent subrange at high wavenumbers / small vertical scales. Wavenumbers indicated on the x-axis correspond to the Kolmogorov scale (k_v), the Ozmidov scale (k_o), and the edge of the quasi-linear internal wave regime (k_c). The blue arrows schematically indicate the direction of energy transfer from large to dissipative scales.

0.2 (Osborn 1980; Oakey 1982). Microstructure instruments, which estimate ϵ by measuring well into the inertial subrange, continue to provide the gold standard for determining diapycnal mixing in the ocean (Gregg 1991; Moum et al. 1995). However, the instruments needed to carry out these measurements are costly, and experienced teams are required to deploy and recover them.

Several methods exist for estimating the dissipation rate by capturing the downscale cascade at an earlier

point in the process, either at the outer scales of turbulent overturns (Sec. 3a) or at the small-scale end of the internal-wave continuum (Sec. 3b). In a steady state this rate of downscale energy transfer is assumed equal to the dissipation rate, and hence can be used to estimate diffusivity. As a general rule, the further one steps back in this Fourier space cascade (the larger the scales used to estimate the dissipation rate), the larger the number of assumptions made and the greater the uncertainty of the diffusivity estimate.

a. Overturns

The outer scales of turbulent overturns can often be measured with standard CTD sensors, provided that the data are saved at a high enough resolution. In stratified turbulence, the outer scale given by Ozmidov scale (Dillon 1982):

$$L_0 = \frac{2\pi}{m_0} = \sqrt{\frac{\epsilon}{N^3}} \sim O(0.1 - 10\text{m}), \quad (2)$$

The observational equivalent is known as the Thorpe scale (L_T), defined as the root mean squared displacement a parcel has moved between a measured density profile with a density inversion (overturn) and the sorted version of the same profile. The Thorpe scale has been shown to be a good estimate of the Ozmidov scale ($L_T \sim L_0$), so CTD measurements of density inversions can be used to estimate ϵ through Eqn.(2) (Thorpe 1977; Dillon 1982; Ferron et al. 1998). The results generally compare well with microstructure estimates (e.g. Seim and Gregg (1994); Ferron et al. (1998); Klymak et al. (2008)). The Thorpe method has been successfully applied to a range of instruments, including shipboard CTDs (Gargett and

Garner 2008), McLane Profiler measurements (Alford *et al.* 2006; Nash *et al.* 2007; Alford 2010; Martini *et al.* 2011), expendable instruments (Thompson *et al.* 2007), and SeaSoar (Martin and Rudnick 2007). Care must be taken though to avoid interpreting noise in density measurements as genuine overturns. Tests to detect spurious overturns are nicely reviewed by Galbraith and Kelley (1996), and discussed further in Section 4a.

b. Finescale parameterization

Stepping to larger scales, the rate of downscale energy transfer through the internal wave field can be estimated by combining finescale measurements (order 10-100 meters) with theoretical models of energy transfer through wave-wave interaction. Many formulations are based on the canonical Garrett-Munk (GM) internal wave spectra of shear and strain, both of which are nearly flat at larger scales, then drop off with a -1 slope beyond a cutoff wavenumber (k_c in Figure 3) (Gregg and Kunze 1991). Physically, motions at scales larger than the cutoff (smaller wavenumbers) are interpreted as weakly nonlinear internal waves, while motions at smaller scales become more strongly nonlinear, eventually leading to wave breaking (D'Asaro and Lien 2000). For the empirically derived GM spectrum, the transition occurs at a wavelength of $k_c = 10$ m. For other observations, the cutoff appears to move towards higher lower wavenumbers with higher spectral energy levels (Garrett 1990). Polzin *et al.* (1995) suggest a family of spectra in which the cutoff occurs at a point in which cumulatively integrated stratification normalized shear variance (essentially an inverse Richardson number) is 0.66, the value the GM spectra achieves at 10 m.

The rate of downscale energy transfer through the weakly nonlinear range, and thus the dissipation rate, tends to scale quadratically with the spectral level (\hat{E}) a scaling consistent between theory (Müller *et al.* 1986; Henyey *et al.* 1986; Lvov *et al.* 2004), observations (Gregg 1989; Polzin *et al.* 1995; Gregg *et al.* 2003), and numerical simulations (Winters and D'Asaro 1997). Henyey *et al.* (1986) physically interpret this transfer rate as the rate at which small-scale waves (with wavenumbers near k_c) are being refracted towards dissipative scales by interaction with larger-scale shear. Following Gregg *et al.* (2003) and K06, the dissipation rate can be written as

$$\varepsilon = \varepsilon_0 \left(\frac{N}{N_0} \right)^2 \hat{E}^2 L(R_w, \theta) \quad (3)$$

where

$$\hat{E}^2 = \frac{\langle U_z^2 \rangle^2}{\langle U_z^2 \rangle_{GM}^2} \left(\frac{1 + 1/R_w}{4/3} \right)$$

$$\langle U_z^2 \rangle = \int^{k_c} \phi_{U_z}(k_z) dk_z$$

$$L(R_w, \theta) = \sqrt{\frac{2}{R_w - 1}} \left[\frac{f \cosh^{-1}(N/f)}{f_{30} \cosh^{-1}(N_0/f_{30})} \right]$$

$$\varepsilon_0 = 6.7310^{-10} \text{Wkg}^{-1}; \quad N_0 = 3 \text{cph}$$

Here \hat{E} represents the level of the internal wave field, specifically the value of the stratification-normalized shear spectrum (ϕ_{U_z}) integrated to a cutoff wavenumber normalized by the canonical Garrett-Munk (GM) spectrum integrated over the same wavenumber range. The cutoff wavenumber (k_c) is calculated by requiring a set value of observed shear variance - we use $\langle U_z^2 \rangle = 0.66$ following Gregg *et al.* (2003). R_w is the shear/strain ratio,

$$R_w = \frac{\langle U_z^2 \rangle}{\zeta_z^2} \quad (4)$$

where ζ_z^2 is the strain variance integrated out to k_c . Here R_w is the shear to strain ratio and provides a measure of the average frequency content of a wavefield. For a GM spectrum $R_w = 3$. The R_w term in \hat{E} accounts for the contribution of potential energy to the total (whereas shear spectra represent the kinetic energy). Conversely, (3) can be written in terms of measured strain instead of shear variance, with a slightly modified $\hat{E}(R_w)$ term (K06). The $L(R_w, \theta)$ term includes the theoretical dependence on downscale energy transfer rate on both average wavefield frequency content (through R_w) and latitude (Polzin *et al.* 1995; Gregg *et al.* 2003).

In ideal circumstances both shear and strain are measured to high vertical resolution. The prescription to apply (3) is then a) determine k_c by integrating the shear spectrum to a prescribed variance, b) calculate R_w by integrating both shear and strain to k_c , c) compute the GM shear variance integrated to k_c , d) plug everything into (3).

Realistically, many observations are limited in one way or another and a modified version of (3) is used. For example, the Lowered ADCP data used by K06 is noisy at scales smaller than about 50 m. They thus calculate the variance term $\langle U_z^2 \rangle$ by integrating out to the highest non-noisy wavenumber, typically lower than the 'real' k_c would be. If the spectra are indeed white out to k_c (Fig. 3), then this yields the same results, but as will be demonstrated below integrating to a lower wavenumber with non-white spectra yields biased results. Other studies attempt to apply the method using measurements of either shear or strain alone, with an assumed value of R_w (Wijesekera *et al.* 1993).

In addition to measurement limitations, finescale parameterizations may be inappropriate where the underlying physics is not as predicted by theory. For example, the type of directly breaking internal tides observed by both Klymak *et al.* (2008) and Alford *et al.* (2011) require no spectral cascade and result in significantly higher dissipation rates than predicted by a finescale model. The method also fails in more subtle ways where downscale energy transfer is influenced by scattering from topography (Kunze *et al.* 2002) or by the limited bandwidth of shallow water (MacKinnon and Gregg 2003).

4. Results

a. Thorpe Scales

The Thorpe method was applied to density data from both the MMPs and the FCTD. Several previous studies have calculated Thorpe scales from temperature measurements, which tend to have lower noise levels (and hence require less vertical smoothing), but the presence of substantial numbers of density compensated intrusions throughout this dataset required the use of density instead. The accuracy of the estimate is limited by instrument noise in the density measurement and the size of resolvable overturns. Here density noise has been limited by smoothing data in depth, so vertical resolution is the primary constraint (Johnson and Garrett 2004). For both instruments (FCTD and MMP), the Thorpe displacement (L_{th}) was computed by subtracting observed from sorted density profiles. The overturn or patch size (L_{ot}) was taken as the region over which $\Sigma L_{th} = 0$, and the Thorpe scale (L_T) the rms of the Thorpe displacement over each patch. Here it is important to use a buoyancy frequency in (2) that is computed from the sorted density profile within each overturn, not an average or smoothed value (Alford and Pinkel 2000). Overturns were only allowed if they met a minimum overturn patch size criteria (2.5m for FCTD and 9m for MMP), satisfied the run length criteria of Galbraith and Kelley (1996), and had density that deviated from the sorted profile by at least twice the instrument noise (Sec. 2).

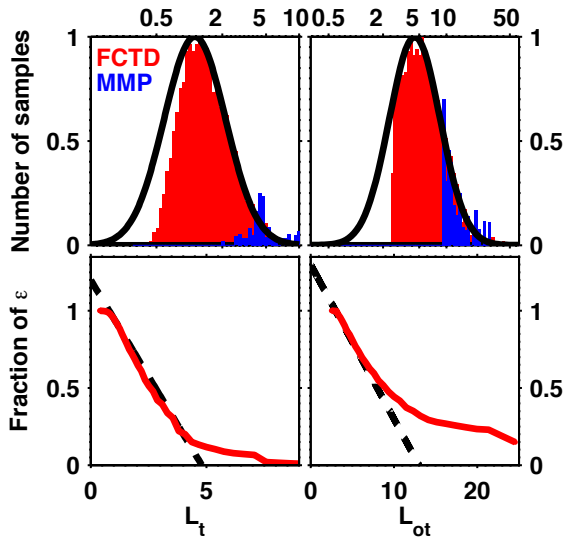


FIG. 4. Overturn statistics for the FCTD and MMP at 29 N (MP3/TS1). Top row: pdfs of distribution of Thorpe scales (left) and overturn patch sizes (right) for FCTD (red) and MMP (blue). The black line is a Gaussian fit assuming a lognormal distribution. Bottom row: the cumulative contribution of overturns with particular classes of Thorpe scales (left) and overturn sizes (right) to total dissipation rate, integrating from large to small scales. The dotted black line in each panel has a y-intercept of 1.2, see text.

A natural question with the method is whether the resolution limitation leads to a significant underestimate of

dissipation from potentially important small overturns. The distributions of Thorpe displacements and overturn patch sizes for the FCTD both look close to lognormal (Fig 4, top panels, red), consistent with Alford and Pinkel (2000). The overturn size limit imposes a sharp cutoff at 2.5 min patch size pdf, and a dropoff in the Thorpe displacement pdf around a meter. Comparison with a gaussian fit (black curve) suggests the FCTD is capturing about 80% of the overturns. The relative importance of each overturn size class can be seen by adding the cumulative contribution of each overturn class to the total dissipation rate, integrating from large (resolved) to small scales (Fig 4, lower panels). The relative contribution is approximately linear with decreasing patch size/displacement for overturns less than 5-6m. This linearity allows an estimate of the unresolved dissipation by extrapolating the line leftwards towards small scales. The resulting intercept is near 1.2, suggesting the FCTD is only missing around 20% of the total dissipation.

For the MMP, the resolution limitation is more serious. Though the FCTD is only sampling for a fraction of the MMP time series, we can roughly estimate the statistical limitations of the MMP data by comparison with the FCTD data. For example, comparison of the patch size PDFs suggests the MMPs are only resolving 15 % of the overturns (Fig. 4, upper panels, blue), and less than a third of the total dissipation. It's worth noting that the severity of this constraint is environment-dependent. For example, Alford (2010) get much better statistics from the a similar instrument due not only to a quieter CTD, but also to lower stratification and a generally higher-energy environment, both of which lead to significantly larger overturns.

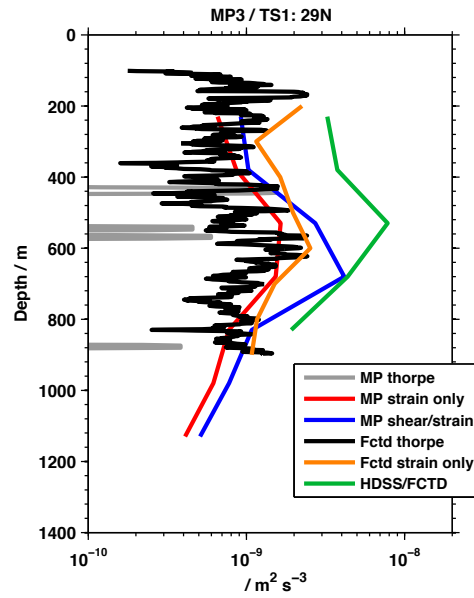


FIG. 5. Average dissipation rate plots at 28.9 N during TS1 from various instruments. Here data are averaged over the 4-day time range during which the Fast CTD was operating.

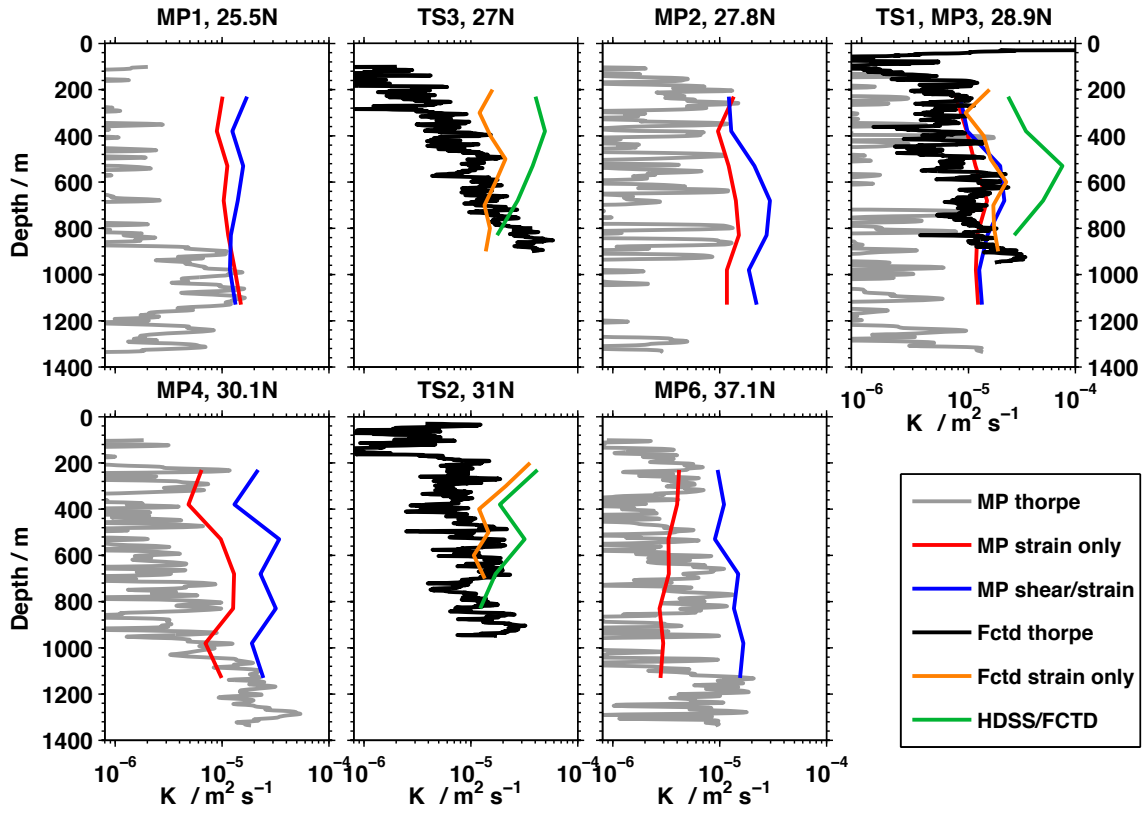


FIG. 6. Average diffusivity plots from all time series, grouped by latitude. The same colors are used in Figures 5, 8, and 9. Here the MMP data were averaged over the entire deployment, while the FCTD and HDSS data were averaged only over the 4 days of each time series.

The time averaged profiles of dissipation rate from the Thorpe scale method for each instrument are shown in Figures 5 and 6 (black versus grey). The only example of co-located MMP and FCTD measurements is at 28.9 N (Fig 5). Here the depth average of dissipation rate from MMP overturns is only 8% that from the FCTD, averaged over the same 4-day time period. When MMP dissipation rates are averaged over the full 50-day time series, the total rises to 14% of the FCTD depth-averaged dissipation rate. This is significantly less than the ratio suggested by the statistical analysis above. The discrepancy is likely due to the smoothing required by the higher noise level, limiting overturn detection at all scales. We therefore conclude that the overturn method does not yield useful results applied to MMP data for this experiment.

b. Finescale measurements

1) METHOD

Since application of finescale diffusivity parameterizations (Sec. 3b) is dependent on assumptions about shear and strain spectra, we start with a closer look at the observed shear and strain. Raw shear data from each mooring are presented in *Pickering et al. (2011)* and will not

be repeated here. Shear spectra for both MMP and HDSS data were computed in half-overlapping 300-meter windows, with the result normalized by stratification ($K06$). Strain spectra were computed from density profiles in the same vertical windows for both FCTD and MMP density. Here strain is taken as $\zeta_z = (N^2 - \bar{N}^2)/\bar{N}^2$ where \bar{N}^2 is a time-averaged profile smoothed over 20 m. All spectra were corrected for high-wavenumber rolloff associated with first differencing.

Example shear and strain spectra from the 4-days of the first FCTD time series are shown in Figure 7. The time-averaged average strain spectra from both the MMP and FCTD are GM-like in both shape and level (upper right panel), whereas average shear spectra have a pronounced peak in the few hundred meter wavelength range (upper left panel). This low-wavenumber shear peak is almost entirely due to near-inertial frequency motions, which can be seen by comparing wavenumber spectra of bandpassed near-inertial (cyan) and super-inertial (magenta) shear (Fig. 8). In other words, the spectra are non-separable in frequency-wavenumber space, violating a fundamental assumption of the Garrett-Munk model. The HDSS shear starts to roll off near 0.01 cpm, a known response of this instrument (R. Pinkel).

Finescale diffusivity estimates from MMP data are cal-

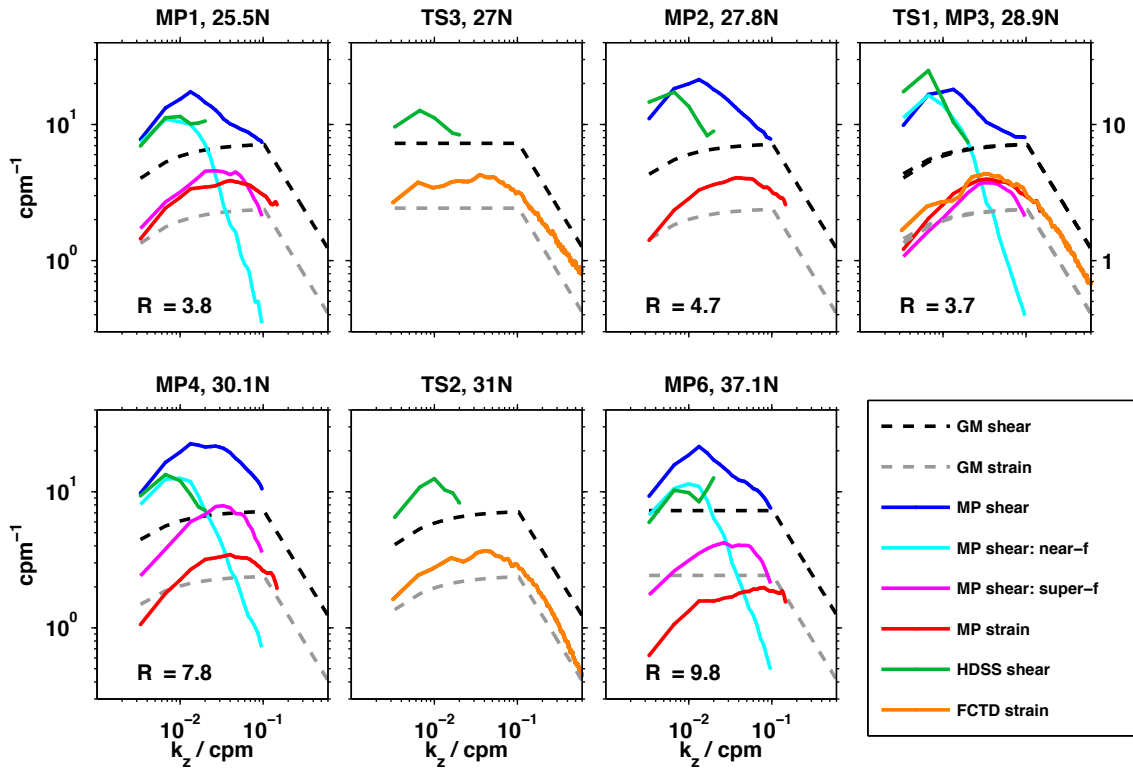


FIG. 8. Spectral comparisons for 5 moorings. Spectra have been depth averaged between 200-1200 meters, and GM levels are indicated with dotted lines. The shear/strain ratio, R_0 was calculated in each case by integrating spectra out to k_c . When possible, bandpassed near-inertial and super-inertial MMP shear are shown as well (at MP2, TS2 and TS3 the time series are not long enough to permit responsible bandpassing)

culated using two methods. First, the full method of (1) and (3) is used, incorporating both shear and strain spectra (Fig. 7, lower left, blue). Second, for comparison with other published work, diffusivity is also calculated from MMP data using a strain-only version of (3). In this case \hat{E} is estimated using strain spectra integrated out to a cutoff wavenumber, k_c , at which cumulative variance is 0.22 (Kunze *et al.* 2006), and an assumed shear/strain ratio of $R_w = 3$ (Fig. 7, lower right, pink). For the HDSS data, shear spectra are integrated to a maximum wavenumber of 0.02 cpm due to instrument resolution limitations; the actual k_c employed is rarely below this value (Fig. 7, left panels, green). For FCTD data, strain-based diffusivity estimates are calculated identically to those from MMP strain data (Fig. 7, right panels, orange).

As the basic state of the internal wave field is not expected to change significantly over this short a time period, the data provide an opportunity to explore the variability of diffusivity estimates calculated from individual spectra. Spectra of both shear and strain vary by 1-2 orders of magnitude over this four-day period, which can be seen in either the plotted individual spectra or equivalently in the range of cutoff wavenumbers used (Fig. 7, upper row).

The resultant variability in diffusivity estimated from individual profiles of either MMP shear or strain spectra

are indicated with histograms in the lower panels of Figure 7. In both cases diffusivity estimates have a factor of ~ 50 range. Also shown are diffusivity estimates computed from time-averaged spectra (solid vertical lines). The strain-based estimates from the MMP and FCTD are very similar (red vs orange, lower right panel), reflecting the encouragingly similar average strain spectra from the two instruments. The HDSS shear diffusivity estimate is biased high compared to that that from MMP shear (green vs blue in lower left panel) owing to the red nature of the shear spectra coupled with the limited wavenumber range used for the HDSS integration.

2) LATITUDINAL PATTERNS

Comparing average strain spectra across all depths and latitudes, observed strain continues to be GM-like (Fig. 8) in both shape and level. The strain spectral level is slightly above GM at lower latitudes, and declines to at or slightly below GM at MP6. Where FCTD and MMP measurements coincide, strain spectral estimates are close (red versus orange in Figure 9). In contrast, shear spectra at all latitudes deviate significantly from the flat GM shape at low wavenumbers, often with a peak at 100-300 meter wavelengths. These peaks are primarily from coherent near-inertial motions (cyan in Fig. 8), attributable to a combination of PSI and wind-generated near-inertial

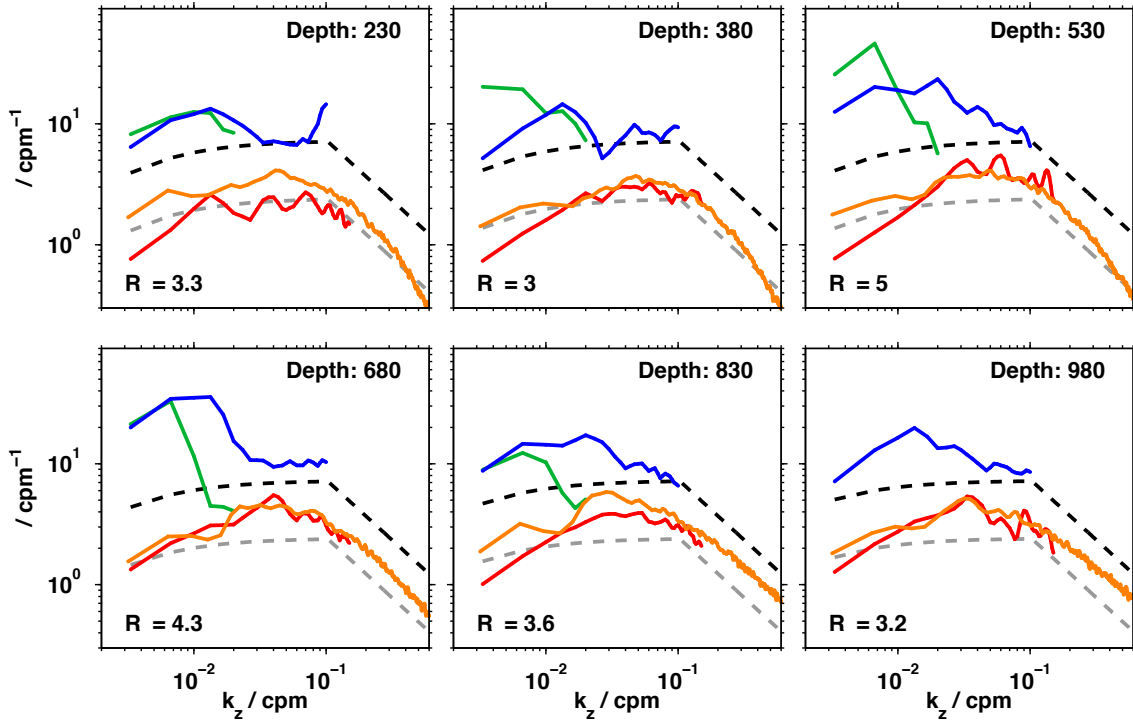


FIG. 9. Spectral comparisons for various depth windows at 28.9 N. Here all data have been averaged over the 4-day period of the TS1 time series. Colors as shown in Fig. 8.

waves (MacKinnon *et al.* 2011; Pickering *et al.* 2011). Reflecting these differences, the shear/strain ratio (R_w) is always greater than the GM value of 3, with a tendency to increase towards higher latitudes (Fig. 8). Where strong near-inertial features appear at a particular depth range (e.g. mid-depth at MP3, see M11a), this is reflected in a large R_w at this depth range (Fig. 9).

3) LONGITUDINAL PATTERNS

Finescale shear from the E-W HDSS section shows considerable lateral variability along 28.8N (Fig. 1). Shear variance shows a clear enhancement at all depths between 197 and 198 E, just to the east of MP3 (Fig. 10). Shear spectra from this section are normalized using the average stratification profile from MP3. The depth and longitude-averaged shear spectrum between 197 and 198E is enhanced at all wavenumbers compared to that at MP3, particularly in the 200-300m wavelength range (Fig. 10). The depth-averaged shear variance between 197 and 198 E is three times that at MP3. Diffusivity is calculated from finescale shear along this passage using an assumed $R_w = 3$ and an upper bound of $k_c = 0.01$. Estimated depth-averaged diffusivity rises to $1 \times 10^{-3} \text{ m}^2 \text{ s}^{-1}$ between 197 and 198, a factor of 30 higher than the depth average at MP3.

5. Discussion and conclusions

The data presented here provide an opportunity to

cross-calibrate different methods of estimating turbulent dissipation and diffusivity. In particular, the finescale method is gaining widespread use and a few comments on its sensitivities are warranted. First, the variability between diffusivity from individual spectra is quite large compared to that calculated from averaged spectra (Fig. 7). The fundamental timescales of the wave-wave interaction theory that underlies the finescale method are days or longer (multiple wave periods), so the appropriate measure of wave energy level \hat{E} is really an average spectra (McComas and Müller 1981a; Henyey *et al.* 1986). Thus the variance exhibited by individual spectra and diffusivities calculated from individual spectra on shorter timescales should be interpreted as noise or uncertainty in the method.

The standard deviation of the log of finescale diffusivity at MP3 is close to 0.5 for all depth bins. This is significantly smaller than the values of 1.2-1.5 reported by Gregg *et al.* (1993), likely because computing spectra over particular depth windows (300 m in this case) essentially already involves averaging over that depth range. Nevertheless, published results of diffusivity calculated from individual profiles should be treated with reasonable caution. Averaging may reduce the uncertainty considerably. In particular, using data presented in Gregg *et al.* (1993) (their Fig. 11) and our observed lognormal standard deviation of $\sigma_{lnE} = 0.5$, 95% confidence intervals require approximately 8 independent samples, which could be taken either as time or space averages. As discussed

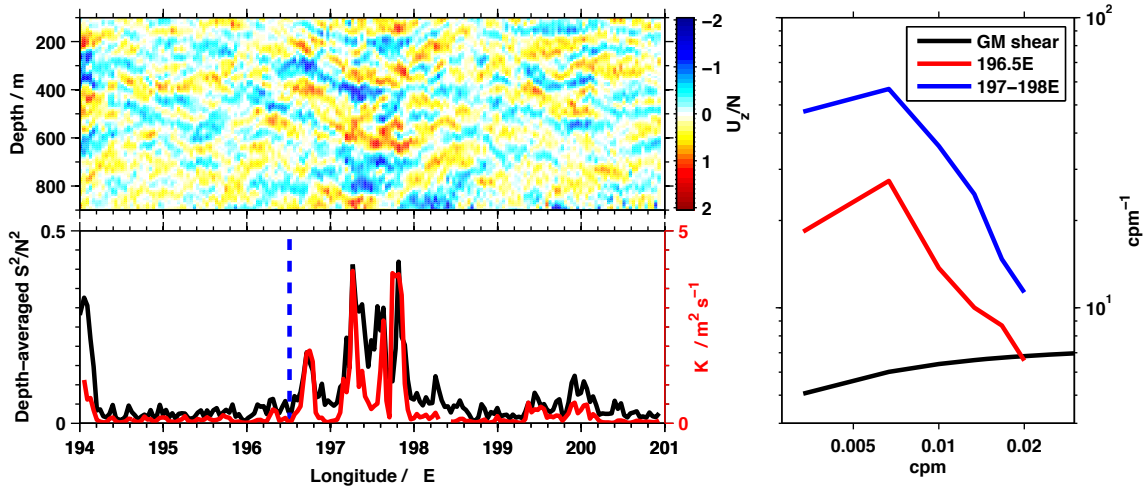


FIG. 10. Upper left: north-south stratification-normalized HDSS shear from the E-W section along 28.8N. Lower left: depth-averaged shear variance for this section (black, left axis) and diffusivity (red, right axis). Right: average shear spectra between 197 and 198 E (blue) and the longitude of MP3, 196.5 E (red)

both by *Gregg et al.* (1993) and more recently by Sun and Pinkel (in prep), independence here requires samples that are separated by typical temporal or spatial decorrelation scales for the internal wave field.

Second, the method is also sensitive to integration limits, particularly when spectra are as red as they are here. For example, diffusivity estimates from HDSS shear are biased high compared to those from MMP shear due to the lower value of k_c used and the red spectral shape (Fig. 7). Comparing all depth bins, the high bias of the HDSS estimate is consistent but not of a uniform magnitude (Fig. 5). In part that's because the spectral shape varies with depth and between stations (Figs. 9, 8). However the situation is complicated by the differing time resolution of the two instruments. In particular, the zig-zag time-depth sampling of the MMP (Fig. 2) means that it observes a subset of the shear observed by the HDSS, so spectra from the two instruments often diverge even in the wavenumber range they're both able to resolve (Fig. 9).

Another consequence of the red, non-separable spectral shape is that diffusivity estimates using shear spectra are generally higher than that from a strain-only method, at least when using an assumed $R_w = 3$. The difference results because the near-inertial motions that comprise the majority of the low wavenumber shear peak do not produce much by way of vertical displacement, and hence do not appear in the strain spectra. The question remains which is a more accurate estimate of mixing rates. During TS1, the only time when we have concurrent measurements of MMP shear/strain and reliable overturns, the strain-only and overturn estimates of dissipation rate are nearly identical (Fig. 5, black versus orange), while the shear-based estimate rises to a factor of 2-3 higher (Fig. 5, blue).

In particular, the shear estimate is higher in the depth

range where shear is dominated by near-inertial motions believed to be from PSI (Fig. 9, M11a), suggesting that the PSI 'daughter' waves are somehow not cascading downscale towards dissipation. On the other hand, the dissipation rates presented here are consistent with the rate of energy transfer through PSI calculated by M11a, arguing that at least a decent percentage of the power going into subharmonic waves is locally dissipated (with the rest radiating equatorwards). Yet the fact that the finescale method overestimates the dissipation rate suggests that the functional relationship between spectral energy level and downscale energy transfer rate is different than that predicted by wave-wave interaction theory. A possible explanation is that near-inertial motions created by PSI (or from recent local storms for that matter) are coherent, while the wave-wave interaction theory assumes a Gaussian incoherent wavefield. Ongoing theoretical and numerical investigations should shed some light on the matter.

Though the mixing methods presented here somewhat disagree with each other, all show a modest step-function increase at and equatorwards of the PSI critical latitude. The implication is that extra shear produced by equatorward propagating PSI-generated near-inertial waves does filter through the spectrum (at its own rate), producing a 2-3 fold increase in mixing rates (Fig. 11) along this particular slice of the Pacific. The shear data from the E-W section suggest that PSI-related mixing might be significantly higher in concentrated beams of tidal energy. Such beams are best interpreted as interference patterns that can shift with changes in the mesoscale features that control tidal ray paths (*Rainville et al.* 2010). The altimetric flux patterns visible in Figure 1 represent only the coherent portion of low-mode tidal flux, essentially the part that remains after shifting interference patterns are averaged over years (*Zhao et al.* 2010). Regional tidal

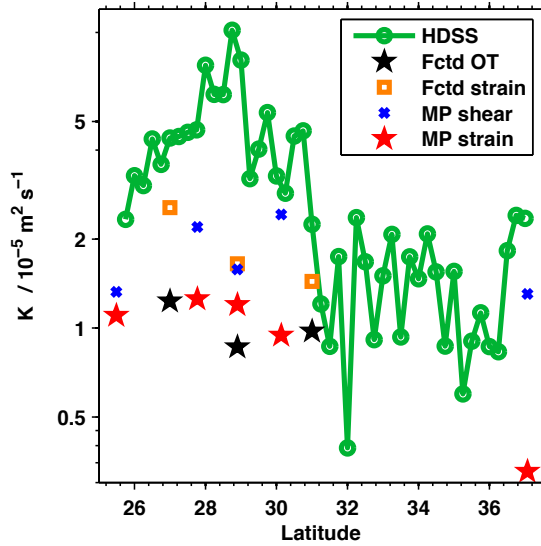


FIG. 11. Depth-averaged diffusivity as a function of latitude for several instruments and methods. HDSS data (green) is from the full N-S ship tracks shown in Fig. 1, with a R_w at each latitude based on interpolation between station values. Other data are station averages at each location.

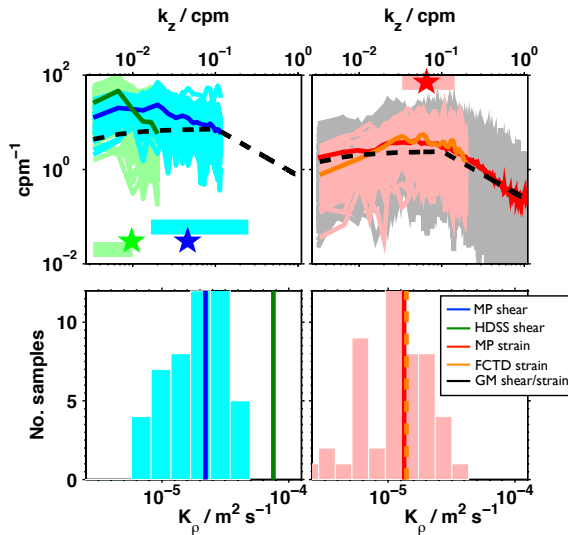


FIG. 7. Example finescale spectra and diffusivity estimates for the four-day time series at TS1. Upper row: all individual shear (left) and strain (right) spectra for the depth bin centered at 530m. Spectra from MMP shear, HDSS shear, MMP strain and FCTD strain are plotted as cyan, green, pink and grey, respectively. Time-averaged spectra are shown with solid lines, with color indicated in the legend. Lower row: histograms of finescale estimates of diffusivity from individual spectra of MMP shear/strain (left, cyan) and MMP strain only (right, pink). Diffusivity estimates from time-averaged spectra from all instruments are shown with solid vertical lines. The range of cutoff wavenumbers, k_c , used in each calculation are shown with horizontal bars in the upper panels, with the average values indicated by stars.

numerical simulations that include different mesoscale states show more focused tidal beams that shift back and forth through the longitude range of enhance shear in Figure 10 (Ed Zaron, pers. comm.).

Overall, the mixing rates presented here are quite modest, often close to GM levels (Fig. 11), supporting the conclusion that mixing in the mid-ocean thermocline is typically weak. Though elevation associated with PSI may be an important mixing pattern to include in global models (Jochum 2009), these rates do not imply a significant drain of energy from the internal tide. Dissipation of the 1-2 TW of power going into the near-inertial and tidal internal wavefields (Wunsch and Ferrari 2004) must be occurring elsewhere.

Acknowledgements.

This work was sponsored by NSF OCE 04-25283. We thank the tireless captain and crew of the R/V Revelle, Tom Peacock, Paula Echeverri, and Kim Martini for making our two months at sea productive and enjoyable.

REFERENCES

- Alford, M., and M. Gregg, Near-inertial mixing: Modulation of shear, strain and microstructure at low latitude, *J. Geophys. Res.*, 2001, in press.
- Alford, M., and R. Pinkel, Observations of overturning in the thermocline: The context of ocean mixing, *J. Phys. Oceanogr.*, 30, 805–832, 2000.
- Alford, M. H., Sustained, full-water-column observations of internal waves and mixing near Mendocino Escarpment, 2010, submitted.
- Alford, M. H., M. C. Gregg, and M. A. Merrifield, Structure, propagation, and mixing of energetic baroclinic tides in Mamala bay, Oahu, Hawaii, *J. Phys. Oceanogr.*, 36, 997–1018, 2006.
- Alford, M. H., J. A. MacKinnon, Z. Zhao, R. Pinkel, J. Klymak, and T. Peacock, Internal waves across the Pacific, *Geophys. Res. Lett.*, 34, 2007.
- Alford, M. H., et al., Energy flux and dissipation in Luzon Strait: two tales of two ridges, *J. Phys. Oceanogr.*, submitted, 2011.
- D’Asaro, E. A., and R.-C. Lien, The wave-turbulence transition for stratified flows, *J. Phys. Oceanogr.*, 30, 1669–1678, 2000.
- Dillon, T. M., Vertical overturns: A comparison of Thorpe and Ozmidov length scales, *J. Geophys. Res.*, 87, 9601–9613, 1982.
- Doherty, K., D. Frye, S. Liberatore, and J. Toole, A moored profiling instrument, *J. Atmos. Ocean. Tech.*, 16, 1816–1829, 1999.
- Ferron, B., H. Mercier, K. Speer, A. Gargett, and K. Polzin, Mixing in the Romanche Fracture Zone, *J. Phys. Oceanogr.*, 28, 1929–1945, 1998.
- Galbraith, P., and D. Kelley, Identifying overturns in CTD profiles, *J. Atmos. Ocean. Tech.*, 13, 688–702, 1996.
- Gargett, A., and T. Garner, Determining Thorpe scales from ship-lowered CTD density profiles, *J. Atmos. Ocean. Tech.*, 25, 1657–1670, 2008.
- Gargett, A. E., Do we really know how to scale the turbulent kinetic energy dissipation rate ϵ due to breaking of oceanic internal waves?, *J. Geophys. Res.*, 95, 15,971–15,974, 1990.
- Gregg, M., The study of mixing in the ocean: A brief history, *Oceanography*, 1991.
- Gregg, M., Estimation and geography of diapycnal mixing in the stratified ocean, in *Physical processes in lakes and oceans*, edited by J. Imberger, Coastal and Estuarine Studies, pp. 305–338, American Geophysical Union, 1998.
- Gregg, M., H. Seim, and D. Percival, Statistics of shear and turbulent dissipation profiles in random internal wave fields, *J. Phys. Oceanogr.*, 1993.
- Gregg, M. C., Scaling turbulent dissipation in the thermocline, *J. Geophys. Res.*, 94, 9686–9698, 1989.

- Gregg, M. C., and E. Kunze, Shear and strain in Santa Monica Basin, *J. Geophys. Res.*, *96*, 16,709–16,719, 1991.
- Gregg, M. C., T. B. Sanford, and D. P. Winkel, Reduced mixing from the breaking of internal waves in equatorial waters, *Nature*, *422*, 513–515, 2003.
- Harrison, M., and R. Hallberg, Pacific subtropical cell response to reduced equatorial dissipation, *J. Phys. Oceanogr.*, *38*, 1894–1912, 2008.
- Heney, F. S., J. Wright, and S. M. Flatté, Energy and action flow through the internal wave field, *J. Geophys. Res.*, *91*, 8487–8495, 1986.
- Hibiya, T., and M. Nagasawa, Latitudinal dependence of diapycnal diffusivity in the thermocline estimated using a finescale parameterization, *Geophysical Research Letters*, *31*, 2004.
- Jayne, S. R., The impact of abyssal mixing parameterizations in an ocean general circulation model, *J. Phys. Oceanogr.*, *39*, 1756–1775, 2009.
- Jochum, M., Impact of latitudinal variations in vertical diffusivity impact of latitudinal variations in vertical diffusivity on climate simulations, *J. Geophys. Res.*, *114*, 2009.
- Jochum, M., and J. Potemra, Sensitivity of tropical rainfall to Banda Sea diffusivity in the Community Climate System Model., *J. Climate*, *21*, 6445–6454, 2008.
- Johnson, H. L., and C. Garrett, Effects of noise on Thorpe scales and run lengths, *J. Phys. Oceanogr.*, *34*, 2359–2372, 2004.
- Johnston, T. S., M. A. Merrifield, and P. Holloway, Internal tide scattering at the Line Islands Ridge, *J. Geophys. Res.*, *108*, doi:10.1029/2003JC001,844, 2003.
- Kelly, S., J. Nash, K. Martini, M. Alford, and E. Kunze, Internal-tide generation and scattering on a continental slope, *J. Phys. Oceanogr.*, 2011.
- Klymak, J. M., R. Pinkel, and L. Rainville, Direct breaking of the internal tide near topography: Kaena Ridge, Hawaii, *J. Phys. Oceanogr.*, *38*, 380–399, 2008.
- Kunze, E., L. K. Rosenfeld, G. S. Carter, and M. C. Gregg, Internal waves in monterey submarine canyon, *J. Phys. Oceanogr.*, *32*, 1890–1913, 2002.
- Kunze, E., E. Firing, J. M. Hummon, T. K. Chereskin, and A. M. Thurnherr, Global abyssal mixing inferred from lowered ADCP shear and CTD strain profiles, *J. Phys. Oceanogr.*, *36*, 1553–1576, 2006.
- Lueck, R. G., and J. J. Picklo, Thermal inertia of conductivity cells: Observations with a Sea-Bird cell, *J. Atmos. Ocean. Tech.*, *7*, 756–768, 1990.
- Lvov, Y. V., K. L. Polzin, and E. G. Tabak, Energy spectra of the ocean's internal wave field: Theory and observations, *Physical Review Letters*, *92*, 128,501–1–4, 2004.
- MacKinnon, J., and M. Gregg, Mixing on the late-summer New England shelf – solibores, shear and stratification, *JPO*, *33*, 1476–1492, 2003.
- MacKinnon, J. A., and K. Winters, Subtropical catastrophe: significant loss of low-mode tidal energy at 28.9 degrees, *Geophysical Research Letters*, *32*, doi:10.1029/2005GL023,376, 2005.
- MacKinnon, J. A., M. H. Alford, O. Sun, R. Pinkel, Z. Zhao, and J. Klymak, Evidence of parametric subharmonic instability of the internal tide 29n, *J. Phys. Oceanogr.*, submitted, 2011.
- Martin, J. P., and D. L. Rudnick, Inferences and Observations of Turbulent Dissipation and Mixing in the Upper Ocean at the Hawaiian Ridge, *J. Phys. Oceanogr.*, *37*, 476–494, 2007.
- Martini, K. I., M. H. Alford, E. Kunze, S. H. Kelly, and J. D. Nash, Observations of internal tides on the oregon continental slope, *J. Phys. Oceanogr.*, in review, 2011.
- McComas, C. H., and P. Müller, Time scales of resonant interaction among oceanic internal waves, *J. Phys. Oceanogr.*, *11*, 139–147, 1981a.
- McComas, C. H., and P. Müller, The dynamic balance of internal waves, *J. Phys. Oceanogr.*, *11*, 970–986, 1981b.
- Moum, J., M. C. Gregg, R.-C. Lien, and M. Carr, Comparison of turbulence kinetic energy dissipation rate estimates from two ocean microstructure profilers, *J. Atmos. Ocean. Tech.*, *12*, 346–366, 1995.
- Müller, P., G. Holloway, F. Heney, and N. Pomphrey, Nonlinear interactions among internal gravity waves, *Rev. Geophys.*, *24*, 493–536, 1986.
- Nash, J., M. H. Alford, E. Kunze, K. Martini, and S. Kelly, Hotspots of deep ocean mixing on the oregon continental slope, *Geophys. Res. Lett.*, *34*, doi:10.1029/2006GL028,170, 2007.
- Nash, J. D., E. Kunze, J. M. Toole, and R. W. Schmitt, Internal tide reflection and turbulent mixing on the continental slope, *J. Phys. Oceanogr.*, *34*, 1117–1134, 2004.
- Oakey, N. S., Determination of the rate of dissipation of turbulent energy from simultaneous temperature and velocity shear microstructure measurements, *J. Phys. Oceanogr.*, *12*, 256–271, 1982.
- Osborn, T. R., Estimates of the local rate of vertical diffusion from dissipation measurements, *J. Phys. Oceanogr.*, *10*, 83–89, 1980.
- Pickering, A., M. Alford, Z. Zhao, J. MacKinnon, R. Pinkel, and J. Klymak, Near-inertial waves during the Internal Waves Across the Pacific Experiment, *J. Phys. Oceanogr.*, submitted, 2011.
- Polzin, K., A heuristic description of internal wave dynamics, *J. Phys. Oceanogr.*, *34*, 214–230, 2004.
- Polzin, K., J. Toole, J. Ledwell, and R. Schmitt, Spatial variability of turbulent mixing in the abyssal ocean, *Science*, *276*, 93–96, 1997.
- Polzin, K. L., Mesoscale Eddy–Internal Wave Coupling. Part I: Symmetry, Wave Capture, and Results from the Mid-Ocean Dynamics Experiment, *J. Phys. Oceanogr.*, *38*, 2556–2574, 2008.
- Polzin, K. L., J. M. Toole, and R. W. Schmitt, Finescale parameterizations of turbulent dissipation, *J. Phys. Oceanogr.*, *25*, 306–328, 1995.
- Rainville, L., T. Johnston, G. Carter, M. A. Merrifield, R. Pinkel, B. Dushaw, and P. Worcester, Interference pattern and propagation of the m2 internal tide south of the hawaiian ridge, *J. Phys. Oceanogr.*, *40*, 311–325, 2010.
- Seim, H. E., and M. C. Gregg, Detailed observations of a naturally occurring shear instability, *J. Geophys. Res.*, *99*, 10,049–10,073, 1994.
- St. Laurent, L., and C. Garrett, The role of internal tides in mixing the deep ocean, *J. Phys. Oceanogr.*, *32*, 2882–2899, 2002.
- St. Laurent, L., H. Simmons, and S. Jayne, Estimating tidally driven mixing in the deep ocean, *Geophys. Res. Lett.*, *29*, doi:10.1029/2002GL015,633.e, 2002.
- Staquet, C., and J. Sommeria, Internal gravity waves: from instabilities to turbulence, *Ann. Rev. Fluid Mech.*, *34*, 559–593, 2002.
- Thompson, A. F., S. T. Gille, J. A. MacKinnon, and J. Sprintall, Spatial and temporal patterns of small-scale mixing in Drake Passage, *J. Phys. Oceanogr.*, *37*, 572–592, 2007.
- Thorpe, S., Turbulence and mixing in a Scottish Loch., *Philos. Trans. R. Soc. London Ser. A*, *286*, 125–181, 1977.
- Wijesekera, H., L. Padman, T. Dillon, M. Levine, and C. Paulson, The application of internal-wave dissipation models to a region of strong mixing, *J. Phys. Oceanogr.*, *23*, 269–286, 1993.
- Winters, K. B., and E. A. D'Asaro, Direct simulation of internal wave energy transfer, *J. Phys. Oceanogr.*, *27*, 1937–1945, 1997.
- Wunsch, C., and R. Ferrari, Vertical mixing, energy and the general circulation of the oceans, *Ann. Rev. Fluid Mech.*, *36*, 281–412, 2004.
- Young, W., Y. Tsang, and N. Balmforth, Near-inertial parametric subharmonic instability, *J. Fluid Mech.*, *607*, 25–49, 2008, submitted.
- Zhao, Z., and M. H. Alford, New altimetric estimates of mode-one M2 internal tides in the Central North Pacific Ocean, *jpo*, *39*, 1669–1684, 2009.
- Zhao, Z., M. H. Alford, J. A. MacKinnon, and R. Pinkel, Long-range propagation of the semidiurnal internal tide from the Hawaiian Ridge, *J. Phys. Oceanogr.*, *40*, 713–736, 2010.

Generated with ametsocjmk.cls.

Written by J. M. Klymak